Advanced Functional Materials

ADVANCED FUNCTIONAL MATERIALS
www.afm-journal.de

RESEARCH ARTICLE

High-Entropy Nanostructured Hydride Network Enables Giant Magnetocaloric Effects and Exceptional Plasticity

Qianzi Yang[1] | Qiang Luo[1] | Jingxian Cui[1] | Bo Sun[1] | Fan Hu[1] | Yusha Luo[1] | Gaopeng Zou[1] | Zhijun Guo[1] | Haoran Zhou[1] | Mingqiang Zhang[1] | Yao Zhang[1] | Shuangxi Song[2] | Baolong Shen[1]

[1]School of Materials Science and Engineering, Jiangsu Key Laboratory of Advanced Metallic Materials, Southeast University, Nanjing, P. R. China | [2]State Key Laboratory of Metal Matrix Composites, School of Materials Science and Engineering, Shanghai Jiao Tong University, Shanghai, P. R. China

Correspondence: Qiang Luo (q.luo@seu.edu.cn) | Zhijun Guo (zj-guo@seu.edu.cn) | Shuangxi Song (songshuangxi@sjtu.edu.cn) | Baolong Shen (blshen@seu.edu.cn)

Received: 6 November 2025 | **Revised:** 7 February 2026 | **Accepted:** 11 February 2026

Keywords: high entropy | magnetocaloric effect | nanostructured glass-hydride network | strength–plasticity synergy

ABSTRACT

Achieving a giant magnetocaloric effect (MCE) with negligible hysteresis and excellent strength–plasticity balance poses a significant challenge due to inherently conflicting trade-offs. Here, we develop a high-entropy nanostructured glass-hydride (HENGH) featuring a percolating nano-hydride network in a glass phase, which achieves an unprecedented combination of giant MCE, near-zero hysteresis, and exceptional mechanical properties. HENGH exhibits a maximum magnetic entropy change of 11.3 J kg^{-1} K^{-1} for a field change of 2 T, 200% higher than the hydrogen-free counterpart. Simultaneously, it achieves a yield strength of 2.2 GPa with over 50% plastic strain, beating the strength–plasticity trade-off. It's revealed that the nanostructured glass-hydride network with competing magnetic orders shifts transitions from 3D Ising to tricritical mean-field behavior, combining giant MCE from first-order transition with minimal hysteresis from second-order one. Moreover, unlike conventional hydrogen embrittlement, hydrogenation here enables a brittle-to-ductile transition via collaborative deformation of nanostructured hydride and glass phases. Specifically, nano-hydride deformation triggers nucleation of the shear transformation zone in the glass phase, while their interaction with shear bands induces their multiplication and hydride's rotation or division. The HENGH system, an emerging subclass of high-entropy materials, achieves an exceptional MCE–strength–plasticity synergy, providing a new platform for multifunctional material design.

1 | Introduction

Magnetocaloric materials underpin an emerging, energy-efficient solid-state cooling technology whose applications range from cryocoolers for quantum computing and space exploration to next-generation household refrigeration [1–3]. The enabling phenomenon, the magnetocaloric effect (MCE), arises from the reversible magnetic entropy change during field-driven alignment or randomization of magnetic moments, with the magnitude governed by the magnetic transition nature (first- or second-order) [4]. Over the past two decades, the quest to maximize MCE has focused on the $(Mn,Fe)_2(P,X)$ systems (X = As, Ge, Si), $Gd_5(Si_2Ge_2)$ compound, $La(Fe,Si)_{13}$-based alloys, Ni-Mn-X Heusler alloys (X = Ga, In, Sn, Sb), and Mn-M-X compounds (M = Co, Ni; X = Si, Ge) with first-order magnetic transition (FOMT) [5–8]. The abrupt magnetostructural transition in these FOMT materials enables a giant MCE under relatively low magnetic fields (≤2 T), which is crucial for efficient magnetic cooling. However, practical magnetic refrigeration applications demand a balanced set of properties, going beyond a giant MCE alone. These balanced properties include minimal thermal and magnetic hysteresis for energy efficiency, and high strength and

plasticity to withstand the stresses induced by field variations and phase transitions, as well as to enable processability for device integration [9]. However, a significant challenge arises because FOMT magnetocaloric materials, despite their giant MCE, often suffer from severe hysteresis and brittleness due to lattice instabilities. This leads to energy dissipation, microcracks, and mechanical failure, thereby failing to meet the balanced property requirements for practical magnetic refrigeration applications.

In contrast, second-order magnetic transition (SOMT) MCE materials (such as some rare earth alloys, molecular-based solids, and rare earth oxides, among others) offer a different set of characteristics [10, 11]. Elemental gadolinium (Gd), a prototypical SOMT example, offers the advantages of negligible hysteresis and relative ease of processing. However, its SOMT nature results in only a moderate maximum magnetic entropy change ($-\Delta S_M^{Max}$) at low magnetic fields. More critically for long-term device reliability, the inherently low yield strength of Gd poses a significant mechanical challenge [7]. Rare-earth oxides, exemplified by the benchmark $Gd_3Ga_5O_{12}$ (GGG) and $Gd_3(Ga_{1-x}Fex)_5O_{12}$ (GGIG), and molecular-based solids, including coordination polymers and metal-organic frameworks, both serve as promising magnetic refrigerants for low-temperature (2–20 K) applications due to their giant MCE [10–12]. However, due to their rigid covalent or ionic frameworks, both material families suffer from mechanical brittleness. Amorphous alloys (AMAs) are promising refrigerants due to their enhanced refrigeration capacity, high strength, and improved magnetic softness. However, their application is constrained by a low-to-moderate $-\Delta S_M^{Max}$ value (3-6 J kg^{-1} K^{-1} for a field change of 2 T for typical Gd-based AMAs) and brittleness from localized shear deformation [13, 14]. The introduction of high entropy to AMAs only modulates the magnetic transition temperature and thermal stability in some cases, but fails to address the intrinsic limitations in $-\Delta S_M^{Max}$ and brittleness [15, 16]. Besides, a recent hydrogenated Gd-based AMA (with isolated, homogeneously distributed nanohydrides in the amorphous matrix) showed giant MCE for a field change of 5 T and enhanced mechanical properties, but its $-\Delta S_M^{Max}$ dropped to 6.1 J kg^{-1} K^{-1} for a field change of 2 T, and the underlying multi-scale mechanisms for the performance enhancement are poorly understood [17]. Thus, a material platform that simultaneously achieves low-field-actuated giant MCE, negligible hysteresis, and excellent strength-plasticity synergy to withstand cyclic magneto-mechanical loads remains an urgent and critical challenge in solid-state refrigeration.

Herein, we report a novel high-entropy nanostructured glass-hydride (HENGH) material characterized by a percolating nanohydride network within a glassy matrix, synthesized via controlled hydrogenation of a high-entropy metallic glass $(Gd_{0.2}Dy_{0.2}Er_{0.2}Co_{0.2}Al_{0.2})_{99.5}Si_{0.5}$ with excellent glass-forming ability [18, 19]. The interplay between the unique percolated network of nanohydrides woven throughout the glassy matrix and the high-entropy effect enables a breakthrough in overcoming the inherent magnetocaloric-mechanical trade-off of conventional FOMT and SOMT MCE materials. The developed HENGH shows a maximal magnetic entropy change of 11.3 J kg^{-1} K^{-1} for a low field change of 2 T (200% above the hydrogen-free glass and the largest value yet reported for any glass-based refrigerant) and simultaneously delivers 2.2 GPa yield strength with over 50% plastic strain. Novel mechanisms underlying these remarkable magnetic and mechanical properties have been revealed. These results resolve the persistent MCE–strength–plasticity trilemma and demonstrate that high-entropy design combined with hydride-glass network engineering can transcend conventional property trade-offs, opening pathways to previously inaccessible multifunctional material regimes.

2 | Results

2.1 | Structural Characterization

The as-prepared high-entropy amorphous alloy (HEAMA) powders show good sphericity (Figure S2a), amorphous structure (Figure S2b,c), and homogeneous distribution of Gd, Dy, Er, Co, Al, and Si elements (Figure S3). After hydrogenation, the XRD pattern shows a shifted amorphous halo without any detectable crystalline peaks, indicating expanded atomic spacing. Correspondingly, DSC analysis (Figure S1d) reveals distinct endothermic and exothermic events after hydrogenation. The HEAMA alloy exhibits a distinct glass-transition event at T_g = 608 K and a subsequent crystallization event at T_x = 635 K [19, 20]. In contrast, the HENGH sample shows a broad endothermic peak (615–675 K) due to hydride decomposition, which obscures the glass transition. Note that the crystallization onset temperature of HENGH is elevated to 670 K in HENGH, due to the compositional change of the amorphous matrix induced by hydrogenation.

The high-resolution transmission electron microscopy (HRTEM) image (Figure 1a) reveals 3–6 nm nanocrystalline clusters embedded in the amorphous matrix of HENGH. Correspondingly, the selected area electron diffraction (SAED) pattern shows diffuse halos and sharp rings indexed to rare earth hydrides (REH_2) nanocrystals. Furthermore, aberration-corrected high-angle annular dark-field scanning transmission electron microscopy (HAADF-STEM) clearly reveals an interconnected hydride network within the amorphous matrix (Figure 1b,c). This nanoscale dual-phase structure is further corroborated by the distinctly broad and bimodal modulus distribution in HENGH (Figure S4), which reflects the enhanced mechanical heterogeneity induced by hydrogenation. As shown in Figure 1b, many relatively bright irregular stripes, approximately 3–6 nm in size, form a labyrinth-like network, serving as the backbone structure, and the dark glassy domains disperse randomly around the backbone network. The labyrinth-like domain structures exhibit topological parallels to the Turing pattern (which is ubiquitous in biological morphogenesis, chemical oscillators, and nanocatalysts) [21, 22]. The disorder-mediated Turing-like network in HEAMA arises from its exceptional glass-forming ability and high thermal stability (T_g = 608 K), which preserves the amorphous matrix during the selective formation of rare earth hydrides at 528 K. The stark contrast in hydrogen affinity between the hydride-forming rare earth constituents (Gd, Dy, Er) and the hydrogen-inert components (Al, Co, Si) gives rise to a pronounced reaction-diffusion dynamic. This dynamic, combined with pronounced lattice distortion and sluggish atomic diffusion due to high-entropy effects [23], stabilizes the Turing-like structure.

The left two images in Figure 1d are the zoomed-in views of regions I and II in Figure 1c, and the right two are the

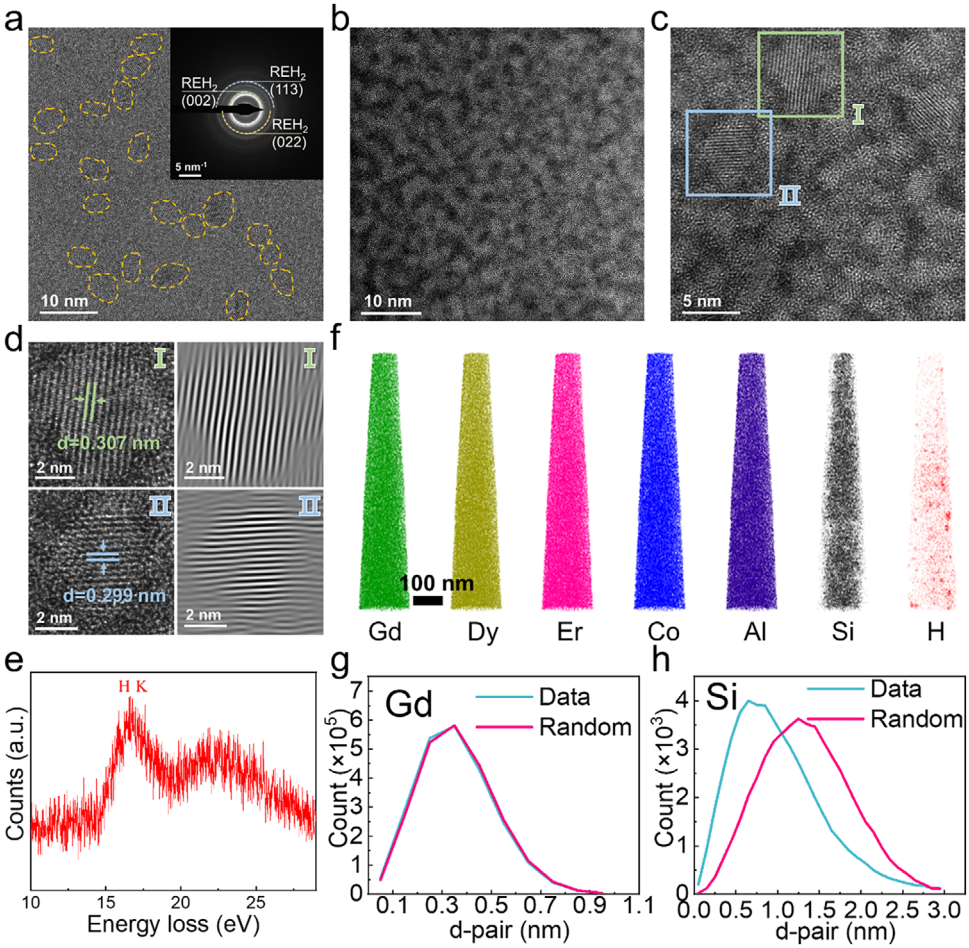

FIGURE 1 | Structure and thermal characterizations of HENGH. (a) HRTEM image and SAED pattern (the inset) of HENGH. Part of the nanocrystals is highlighted with yellow circles. (b and c) HAADF-STEM images. (d) Enlarged view of regions I and II in (c) and the corresponding IFT images. (e) EELS curves of the regions in Figure S5 (local ordering structure). (f) 3D-APT mappings of Gd, Dy, Er, Co, Al, Si, and H elements. (g and h) NND analysis of Gd and Si elements.

corresponding inverse Fourier transform (IFT) images, respectively. The d-spacings in regions I and II are 0.307 nm and 0.299 nm, respectively, corresponding to the (111) crystal plane of GdH_2 and DyH_2 (ErH_2). The IFT images reveal significant lattice distortion, which arises from the combined effects of atomic size mismatch due to high-entropy and local strain fields induced by hydrogen interstitials [23, 24]. Electron energy loss spectroscopy (EELS) was further used to characterize the structurally ordered regions (Figure S5). The hydrogen K-edge EELS spectrum exhibits a characteristic peak at 16.6 eV (Figure 1e), confirming the formation of rare-earth hydride [25]. Additionally, the distinct distributions of elements are elucidated by atom probe tomography (APT) and nearest-neighbor distance (NND) analysis (Figure 1f–h and Figure S6). The Si-Si NND distribution shows a pronounced leftward shift with a peak at ~0.65 nm, revealing the formation of Si-rich nanodomains. This chemical heterogeneity originates from the strongly negative enthalpy of mixing between Si and the rare-earth (Gd, Dy, Er) constituents (Figure S7) [26], which thermodynamically drives Si to preferentially segregate towards RE-rich regions. These chemical fluctuations may seed embryonic crystal-like order and raise the crystallization onset temperature. In contrast, the NND distributions for Al, Gd, Dy, and Er all align with the binomial reference, indicating a statistically random distribution, contributing to the overall stability of the remaining glassy phase.

2.2 | Magnetocaloric Properties and Critical Behavior Analysis

Figure 2a presents FC and ZFC magnetization curves for HEAMA and HENGH. HEAMA bifurcates near 32 K, arising from interplay between the magnetic exchange interaction and strong random magnetic anisotropy (RMA) imposed by the rare-earth (RE) elements Dy and Er [27, 28]. In contrast, the discrepancy between the ZFC and FC curves of HENGH at a lower transition temperature (~5 K) is mainly ascribed to the formation of antiferromagnetic (AFM) hydrides. The significant decrease in the magnetic transition temperature upon hydrogenation can be attributed to the formation of GdH_2, DyH_2, and ErH_2 nanocrystals. The magnetic transition temperatures we determined for single-phase hydrides ErH_2 (4 K), GdH_2 (4 K), and DyH_2 (18 K) (Figure S8) are consistent with those observed in HENGH. Further, Curie-Weiss analysis yields (inset of Figure 2a) paramagnetic Curie temperatures of θ_P = 12 K and −21 K for HEAMA and HENGH, respectively, evidencing a switch from predominant

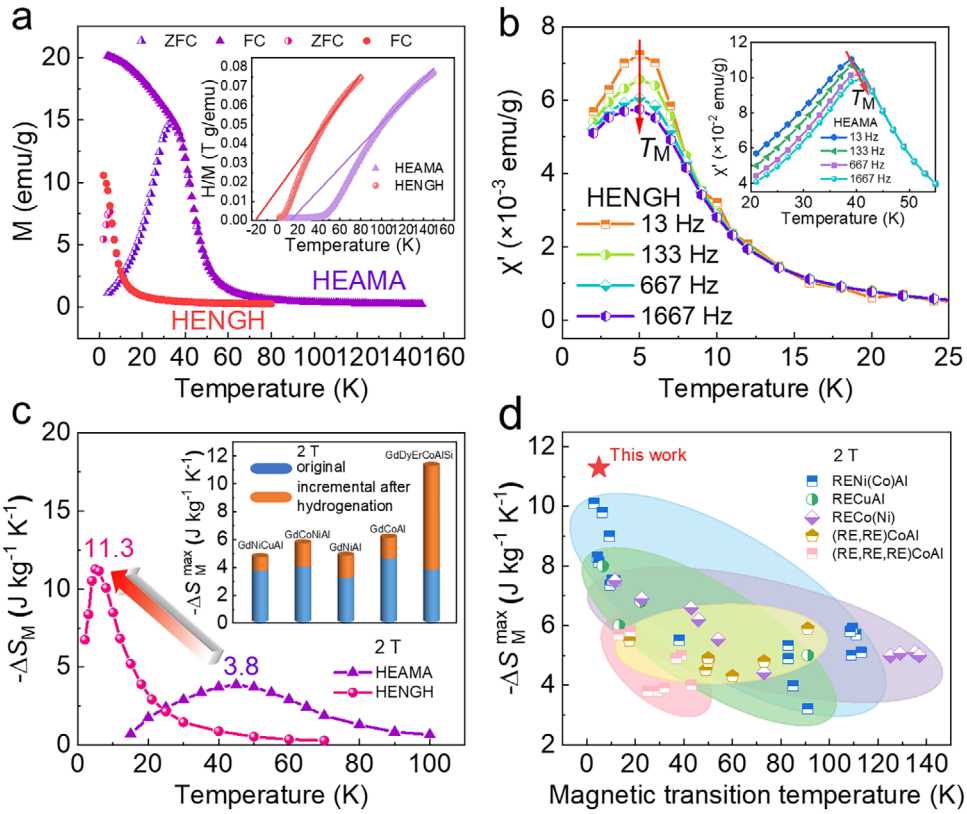

FIGURE 2 | Magnetic transition and magnetocaloric effect of HEAMA and HENGH. (a) ZFC and FC curves of the HEAMA and HENGH powders. The inset shows the Curie-Weiss fitting of the magnetization (M)-temperature curves. The inverse susceptibility $\chi^{-1}(T)$ curve is linear and conforms to the Curie-Weiss law $\chi^{-1}(T) = \mathrm{H/M} = (\mathrm{T}\text{-}\theta_p)/\mathrm{C}$. (b) Temperature dependence of AC magnetic susceptibility (real part, χ') varying from 13 to 1667 Hz for the HENGH. The inset shows the HEAMA. (c) Temperature dependence of magnetic entropy change (ΔS_M) for a field change of 2 T. The inset shows a comparison of maximum magnetic entropy change ($-\Delta S_M^{Max}$) ($\Delta H = 2$ T) for the GdNiCuAl, GdCoNiAl, GdNiAl, GdCoAl, and GdDyErCoAlSi) AMAs before and after hydrogenation. (d) Summary of maximum magnetic entropy change ($-\Delta S_M^{Max}$) (magnetic field change $\Delta H = 2$ T) vs. the magnetic transition temperature (T_M) for the typical amorphous alloys, as well as the value of HENGH.

ferromagnetic to antiferromagnetic order. The hydrogenation fundamentally alters the exchange interaction between RE atoms through lattice expansion and transfers charge from RE to hydrogen. This lattice expansion increases RE-RE distances while the charge transfer drastically reduces itinerant electron density. The severe loss of conduction electrons weakens the original ferromagnetic Ruderman–Kittel–Kasuya–Yosida interaction and allows an antiferromagnetic coupling between RE atoms to emerge. Besides, hydrogenation depletes RE content in the remaining amorphous matrix, leaving a CoAl-rich amorphous matrix that exhibits weak ferromagnetism or paramagnetism. Consequently, the low temperature behavior is dominated by the antiferromagnetic contribution from the RE hydride phases. Figure 2b shows a frequency-independent magnetic-ordering temperature T_M~5 K for HENGH, consistent with typical antiferromagnetic order, whereas HEAMA (inset of Figure 2b) exhibits a frequency-dependent T_M reminiscent of spin-glass-like freezing [29]. Figures S9 and S10 show the isothermal M–H curves and Arrott plots, respectively. The features in the M–H and Arrott plots of HENMA are typical for rare-earth-based AMAs with strong RMA [30]. In contrast, the smooth, non-metamagnetic shape of the M–H curve for HENGH indicates a distinct magnetic state. This is because the formation of dispersed nano-hydride clusters (~3–6 nm) confines AFM correlations within these isolated regions, thereby suppressing long-range AFM order and preventing a collective metamagnetic transition. Subsequent critical scaling analysis reveals fundamentally distinct critical behaviors between HEAMA and HENGH, as evidenced by their respective critical exponents. HEAMA (having critical exponents $\beta = 0.379$, $\gamma = 1.239$, and $\delta = 3.72$) follows the 3D Ising model [31], while HENGH (having critical exponents $\beta = 0.223$, $\gamma = 0.879$, and $\delta = 4.9$) follows the tricritical mean-field model (Figures S11, S12, and Table S1) [32]. In HEAMA, the 3D Ising criticality stems from RMA-controlled spin dynamics, where the strong RMA induced by Dy/Er atoms dominates over the Ruderman-Kittel-Kasuya-Yosida interactions. In contrast, the nanostructured glass-hydride architecture of HENGH establishes a magnetic landscape characterized by competing antiferromagnetic order and weak ferromagnetic interactions, driving the system toward a critical regime that approaches a mean-field tricritical point. This unique critical regime is responsible for the simultaneous achievement of a large magnetic entropy change (characteristic of first-order-like behavior) and minimal hysteresis (inherent to second-order transitions). The observation of well-defined tricritical exponents in this complex system demonstrates how quenched disorder and frustrated interactions can conspire to stabilize a novel criticality, thereby reshaping the magnetocaloric response [33].

Figure 2c shows the magnetic entropy change derived from M-H curves. Hydrogenation boosts $-\Delta S_M^{Max}$ from 3.8 to 11.3 J kg^{-1} K^{-1}

(accompanied by a significant decrease of T_M) for a field change of 2 T (the MCE performances for a field change of 5 T are shown in Figure S13). This gain far exceeds that in hydrogenated Gd-based AMAs (inset of Figure 2c), hydrogenated $Gd_{55}Co_{17.5}Al_{27.5}$, for instance, rises only from 4.7 to 6.1 J kg^{-1} K^{-1} for a field change of 2 T. A direct comparison of the $-\Delta S_M^{Max}$ (2 T) between the HENGH alloy and representative Gd-, Tb-, Ho-, Er-, and Tm-based AMAs is presented in Figure 2d, alongside a configurational entropy-dependent analysis in Figure S14 [34–55]. Our study focuses on overcoming the brittleness and limited MCE of amorphous refrigerants, therefore the comparison is confined to amorphous and amorphous-nanocrystalline systems, excluding crystalline giant-MCE compounds. The giant MCE of HENGH at low magnetic fields enables the development of compact magnetic refrigeration devices that operate with permanent magnets instead of bulky superconducting coils. Another crucial criterion for assessing MCE of magnetocaloric materials is the adiabatic temperature change (ΔT_{ad}). Figure S15a shows the temperature dependence of the specific heat capacity (C_p) of HENGH. A sharp inflection can be observed in the zero-field specific heat capacity curve, indicating a phase transition at 3.8 K. Figure S15b presents the temperature dependence of ΔT_{ad} of the HENGH under a field change of 2 T. The peak value of ΔT_{ad} for the HENGH is calculated as 5.2 K for a field change of 2 T. Moreover, HENGH shows negligible coercivity against HEAMA's pronounced hysteresis (Figure S16), which is a prerequisite for efficient magnetic cooling. Besides, both HEAMA and HENGH obey the scaling law (Figure S17), revealing an intrinsic scale invariance that is insensitive to their differing critical exponents and symmetries.

2.3 | Mechanical Properties

Remarkably, micropillar compression tests reveal an excellent synergy between strength and plasticity induced by hydrogen (Figure 3a), as further evidenced by its in-situ deformation behavior (Video S1). The yield strength determined from Figure 3a increases from 1.2 GPa in HEAMA to 2.2 GPa in HENGH. Concurrently, the plastic strain improves from approximately 10% to over 50% without fracture. Besides, HENGH exhibits pronounced work hardening (inset of Figure 3a) that persists to a plastic strain of approximately 21%, driven primarily by the interaction of shear bands (SBs) with nanoscale hydrides. Beyond ~21% strain, strain softening stems from the accelerated free-volume accumulation within the SBs. A comparison of the strength-ductility performance between HENGH and representative magnetocaloric material systems, including $LaFe_{11.5}Si_{1.5}$, $Gd_3Ga_5O_{12}$ (GGG), $Gd_5Si_2Ge_2$, $GdCo_2$ micropillars, and bulk GdSiGe, LaFeSi, NiMnCo, MnFeP, and rare-earth AMA families, is shown in Figure 3b [5, 6, 56–71]. As the figure indicates, all the typical giant-MCE materials exhibit low strength or poor plasticity (Figures S18–S20 and Videos S2–S4). It is particularly noteworthy that the hydrogen-induced synergy between strength and ductility stands in contrast to the hydrogen embrittlement phenomenon commonly observed in high-strength alloys, including high-strength steels, titanium alloys, aluminum alloys, and Zr-based AMAs [72–74]. Further insight into the deformation mechanisms can be obtained by examining the shear banding behavior, as directly observed in SEM images (Figure 3c–f). In the brittle HEAMA, parallel primary SBs oriented at ~45° with significant cracking produce large, distinct serrations, each marking a major unstable slip event that leads to embrittlement. In contrast, the ductile HENGH exhibits multiple primary SBs accompanied by a high density of secondary SBs, which effectively distribute the plastic strain. The operation of these numerous, smaller bands results in frequent but minor load drops, thereby suppressing the runaway instability associated with a single dominant SB and significantly enhancing ductility. In addition, the in-situ tension test (Figure S21 and Video S5) of HENGH demonstrates ~10% tensile strain, underscoring the hydrogen-engineered ductility. This tensile deformability, rarely achieved in brittle giant-MCE compounds, corroborates micropillar data and establishes HENGH as a rare example of a magnetocaloric material combining giant MCE with damage-tolerant mechanical performance.

Microstructure investigation of the compressed HEAMA and HENGH samples (Figure S22 and Figure 4a–c) was further carried out to elucidate the deformation mechanisms. It can be seen from the HRTEM image that a single primary SB along the direction of the largest shear stress (oriented ~45° to the loading axis) is observed in HEAMA (Figure S22), whereas two parallel primary SBs (widths ~15 nm and 45 nm) accompanied by secondary SBs (Figure 4a) are observed in HENGH. Besides, it is observed that nanocrystals inside the SBs are marginally larger than those outside (Figure 4b). And some hydride nanocrystals within the shear zone are divided by the shear stress (Figure 4c) and subsequently rotated by 28° or 58°. This nanoscale fragmentation and reorientation of hydrides dissipate substantial strain energy and create local stress fields that effectively impede SBs' propagation and promote stable and distributed plastic flows. In addition, a dark-contrast region is observed at the SB intersection (Figure 4d). Energy-dispersive profiling (Figure 4e; S23) further shows that this contrast arises from pronounced Er enrichment concomitant with Co and Al depletion, consistent with elemental re-distribution previously reported in AMAs [75]. Autocorrelation-function (ACF) analysis of the HRTEM image was further carried out to quantify the areal fraction of crystal-like-order (CRL) regions. From the resulting maps, two distinct local structures can be identified. The first yields a maze-like ACF pattern accompanied by a halo FFT, signifying a fully disordered local structure (upper panels in Figure 4f). The second displays well-defined fringes with diffraction spots in the FFT, evidencing crystalline-like symmetry (lower panels in Figure 4f). The CLO area fraction in the compressed HENGH is determined to be ~35% within SBs (Figure 4h) and ~11% outside (Figure 4g), but remains below the pre-deformation value of ~53% (Figure S24). Stress concentrations at hydride-glass interfaces promote nanocrystal amorphization via lattice distortion and bond breaking, lowering overall crystallinity. The locally elevated CLO content within the SBs is attributed to transient temperature rises and intense shear strains that promote nucleation of nanocrystals [76].

3 | Discussion

To elucidate the underlying mechanisms, we demonstrate how the glass-hydride dual-phase nanostructure in HENGH simultaneously achieves a giant magnetocaloric effect and an exceptional synergy of strength and plasticity. Firstly, the formation of a percolating rare earth hydride network alters the magnetic transition from paramagnetic-to-RMA to paramagnetic-

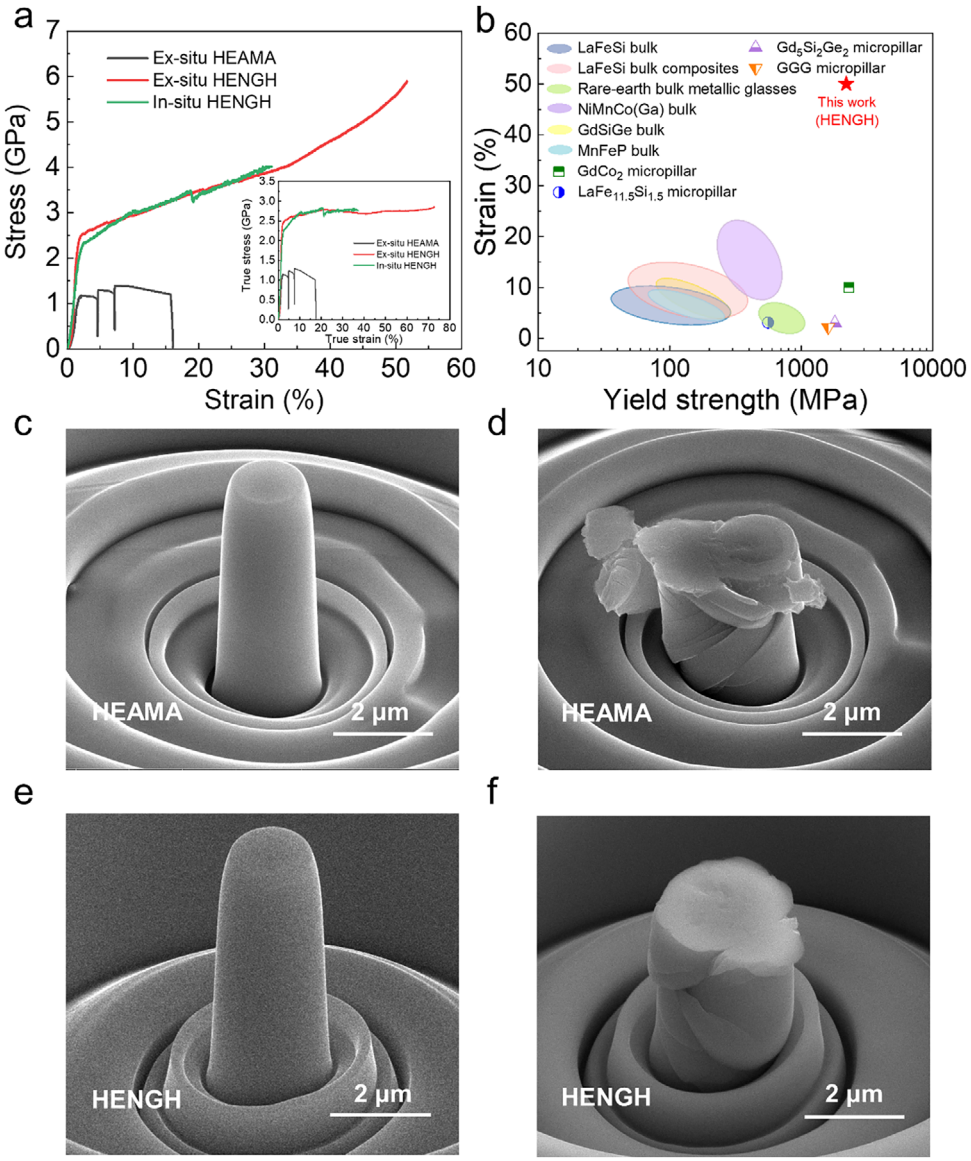

FIGURE 3 | Mechanical properties of the HEAMA and HENGH micropillars. (a) Stress-strain of the pillars with a diameter of 2 μm. The black and red curves show the ex-situ stress-strain of the HEAMA and HENGH micropillars, respectively, and the green curve shows the in-situ stress-strain of the HENGH micropillar. The inset shows the true stress-strain curves of the pillars. (b) Summary of strain vs. yield strength for the typical magnetocaloric materials alloys, as well as the value of HENGH. (c–f) Morphology images before and after compression of HEAMA and HENGH micropillars with a diameter of 2 μm.

to-antiferromagnetic. Unlike HEAMA, in which the broad distribution of exchange interaction and RMA exists due to the amorphous structure, nanocrystalline hydrides exhibit antiferromagnetic interactions with a narrow distribution of exchange constants leads to a sharp, cooperative magnetic transition, which is essential for a large magnetic entropy change [77]. And we find that hydrogenation does not alter the effective magnetic moment, indicating its negligible contribution to the observed MCE enhancement. Moreover, interfacial effects between the nanoclusters and the glassy matrix may contribute to magnetic frustration and broaden the temperature range of the magnetocaloric effect. And the antiferromagnetic nanohydride network, synergizing with high-entropy-driven complex magnetic interactions, induces a crossover from 3D Ising to tricritical mean-field behavior in magnetic transitions [78]. The unique tricritical point, occupying the boundary between first- and second-order transitions, suppresses spin fluctuations via competing orders, thereby enabling a steep yet hysteresis-free magnetization response near the critical point. Consequently, this criticality merges the giant magnetic entropy change of a first-order-like transition with the reversibility of a second-order one, explaining the unprecedented magnetocaloric enhancement (giant MCE with negligible hysteresis) in HENGH [33].

In contrast to single-phase nanocrystals that usually suffer Hall-Petch breakdown at the finest grain sizes [79], HENGH employs an interpenetrating dual-phase architecture of glassy domains and nanoscale hydrides, enabling three synergistic strengthening mechanisms. Firstly, the hydrides, which possess a higher modulus than the glassy domains, can bear a larger proportion of the

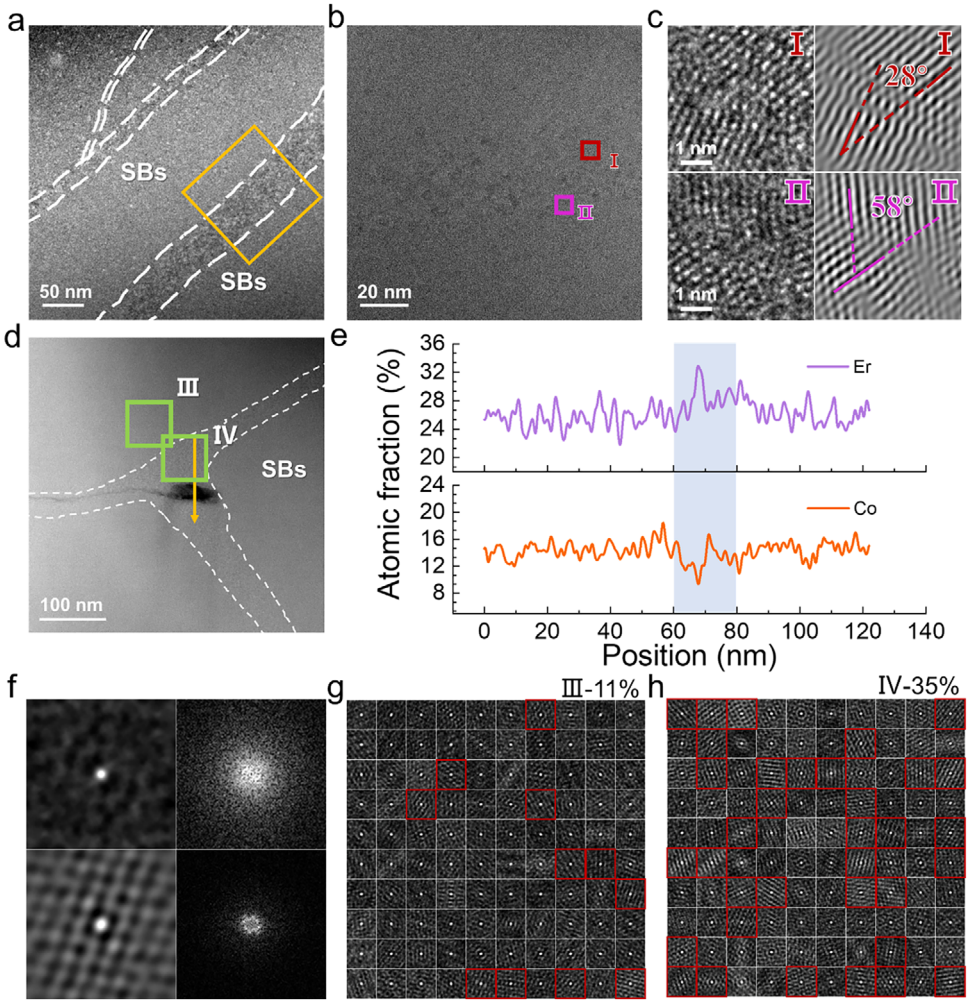

FIGURE 4 | Structure of the HENGH micropillars after compression. (a) Dark-field image of the SBs. (b) HRTEM image of one of the shear bands corresponding to the yellow square of (a). (c) Enlarged view of the marked nanocrystalline regions (I and II) in (b) and the corresponding IFT patterns. (d) HAADF-STEM image of the SBs. (e) The elemental atomic fraction profiles along the line that crosses the shear band in (d). (f) Autocorrelation patterns (left two) showing the features of the wholly disordered and crystal-like-order local structures, and their corresponding FFT patterns (right two). (g and h) 2D autocorrelation maps of HENGH after compression corresponding to the III and IV regions in (d).

applied load [80]. This delays the onset of plasticity in the glassy domains, thereby elevating the yield strength of the composite. Additionally, the nanoscale hydrides act as physical barriers that hinder the rapid propagation of SBs, thereby enhancing strain delocalization and requiring a higher applied stress to cause macroscopic failure. Secondly, because prior studies have reported that nanoscale metallic glasses approach ideal strength by suppressing external flaws and internal defects, thereby delaying shear banding [81], the nanoscale glassy domains in HENGH can likewise attain near-ideal strength, which is conferred on the entire composite. Moreover, the dense amorphous-hydride interfaces provide strong pinning sites for shear-transformation-zone (STZ) activation, increasing the energy barrier for localized shear events and disrupting the cooperative operation of STZs [82]. Collectively, these mechanisms push the material beyond conventional strength limits of rare-earth-based AMAs.

The same Turing-like architecture simultaneously unlocks exceptional ductility. A 35% dispersion of 3–6 nm hydrides creates an interpenetrating glass/hydride network with high-density interfaces, promoting synergistic deformation between the nanostructured glass and hydrides. The hydride spacing (~3–6 nm) matches the STZ size of typical Gd-based AMAs (~6 nm) and is well below the plastic-zone length [17], seeding multiple embryonic SBs rather than a single catastrophic SB in the nano-sized glass phase. Given that the hydrides are harder than the amorphous matrix, they are unlikely to act as primary sites for initiating STZs. Instead, nano-hydrides primarily serve as obstacles that homogenize stress distribution and delay shear localization. Their nanoscale dispersion creates a dense network of stress obstacles, which impedes the formation and propagation of primary shear bands. This promotes the activation of multiple, secondary shear bands throughout the matrix. And the SB-hydride interactions may fragment and rotate the hydride nanodomains, simultaneously enhancing plasticity and strain hardening. In the sub-10-nm regime (3–6 nm here), where dislocation nucleation and motion are inhibited, the hydrides accommodate strain chiefly through lattice distortion and interface-mediated atomic shuffling, analogous to processes in ultra-fine-grained metals [83, 84]. Crucially, the stress field

generated by such deformation in the hydrides can directly nucleate STZs in the adjacent glass, while propagating SBs from the glass conversely drive further shuffling or distortion in the hydrides. This establishes a dynamic, inter-phase synergistic deformation mediated via the hydride-glass interfaces that enhances both strength and plasticity. The size and dispersion of these hydride nanocrystals are critical, as they directly control the density of such active interfaces and the effectiveness of coordinated shear-strain accommodation. Notably, the nanocrystal size and dispersion achieved here (tunable via hydrogenation conditions) appear to reside within an optimal window that concurrently enables a giant MCE and an exceptional strength-ductility combination.

4 | Conclusions

In summary, this work demonstrates that a novel high-entropy glass-hydride architecture can simultaneously achieve a remarkable combination of a giant MCE, negligible hysteresis, and excellent strength-plasticity balance, opening new avenues for advanced material design. This breakthrough originates from the distinctive Turing-like nanostructure. Specifically, the formation of a percolating nano-hydride network not only transforms the magnetic transition from paramagnetic-to-RMA to paramagnetic-to-antiferromagnetic with sharp magnetization changes near T_M, but also creates high-density interfaces to enable collaborative deformation of glass and hydride phases. The structural and magnetic coordination ultimately yields an exceptional MCE–strength–plasticity synergy while avoiding hydrogen embrittlement. Given these multifunctional attributes, we anticipate that this high-entropy hydride material holds promise for energy-efficient magnetic refrigeration, such as cryogenic cooling in quantum computing and space technology, as well as for broader energy-conversion and storage technologies. The indispensable next step toward application is to engineer these powders into structured, porous monoliths with tailored micro-architecture. This can be accomplished by consolidating the hydrogenated powder via techniques such as spark plasma sintering or hot pressing under carefully optimized conditions.

5 | Experimental Section

5.1 | Fabrication of Nanostructured High-Entropy Metallic Glass-Nanohydride Network

$(Gd_{0.2}Dy_{0.2}Er_{0.2}Co_{0.2}Al_{0.2})_{99.5}Si_{0.5}$ master alloy was prepared by arc-melting in an argon atmosphere using a mixture of pure Gd, Dy, Er, Co, Al, and Si. The purity of the Gd, Dy, Er elements was better than 99.9%, and the purity of the Co, Al, and Si elements was better than 99.99 wt.%. $(Gd_{0.2}Dy_{0.2}Er_{0.2}Co_{0.2}Al_{0.2})_{99.5}Si_{0.5}$ master alloy with an excellent glass-forming ability can be easily processed into powder via gas atomization. The as-prepared high-entropy amorphous alloy (HEAMA) powders were produced by gas atomization and then sieved to 54–60 μm for hydrogenation. Hydrogenation was conducted isothermally at 255°C under a hydrogen pressure of 5 MPa for 10 h in a Sieverts-type apparatus (Advanced Materials Corporation, No. 0360Q), yielding powders with a hydrogen content of 1 wt.% (Figure S1).

5.2 | Structural Characterization

The structure of the powders was characterized by Cu-Kα radiation X-ray diffraction (XRD, Rigaku SmartLab9k). The High Angle annular dark field was investigated by a spherical aberration-corrected transmission electron microscopy (HAADF-STEM, Thermo Fisher Spectra 300). Focused ion beam (FIB, Thermo Fisher Helios 5UX) was used to prepare the TEM samples. Electron energy loss spectroscopy (EELS) was used to analyze hydrogen in the sample. The high-resolution transmission electron microscopy was characterized by transmission electron microscopy (TEM, Talos F200X). High-angle annular dark field (HAADF) was recorded using a probe semi-convergence angle of 10.5 mrad and collection semi-angle of 72–200 mrad. Elemental mappings of the samples were acquired by energy-dispersive spectroscopy (EDS). A three-dimensional atom probe (3D-APT) test was carried out to analyze the precipitates using a local electrode atom probe (CAMECA LEAP 4000X HR). The APT specimens were analyzed in a voltage-pulsed mode at about 50 K. The pulse repetition rate and laser energy of the specimen were set to 200 kHz and 60 pj. The 3D reconstructions and composition analysis were undertaken by the Imago visualization and analysis software (IVAS 3.6.8). The APT specimens were prepared by electrolytic polishing at 5–15 V. The morphology of the powders was characterized by scanning electron microscopy (SEM, FEI Sirion 200). The glass transition temperature T_g and crystallization temperature T_x were obtained using differential scanning calorimetry (DSC, Netzsch DSC404F3) at a heating rate of 20 K/min.

5.3 | Magnetocaloric and Mechanical characterization

The temperature and field dependence of DC magnetization were measured using a SQUID magnetometer (MPMS, Quantum Design). The field cooling (FC) magnetization was measured on the heating course after initial cooling from room temperature to 2 K with an applied magnetic field of 0.01 T. The zero-field cooling (ZFC) magnetization was measured on the heating course under the same magnetic field after cooling the sample from room temperature to 2 K with zero field. Isothermal magnetization curves were measured with a varying magnetic field increasing from 0 to 5 T at different temperatures ranging from 2 to 150 K. AC susceptibility was measured at frequencies ranging from 13 to 1667 Hz with an amplitude of 5 Oe using a physical properties measurement system (PPMS 6000, Quantum Design). Specific heat capacity measurements were performed on a physical property measurement system (PPMS, DynaCool, Quantum Design) with a heat capacity option. The 2D maps of the reduced elastic modulus (Er) with a spacing of 500 × 500 nm^2 on the surface of the samples were performed by atomic force microscopy (AFM, Bruker). Micropillars of HEMGH were fabricated with an FIB. Each micropillar's aspect ratio (height/diameter) was set as 2 with a diameter of 2 μm. Ex-Micro-compression and In-Micro-compression tests were conducted at room temperature under displacement-control mode and at a strain rate around 2×10^{-3} s^{-1} (Bruker Ti-950/Bruker PI-89). In situ TEM tensile experiment was investigated by in situ MEMS-STM-TEM multi-field measurement system.

Author Contributions

Conceptualization: Q.L. and B.L.S., methodology: Q.Z.Y., J.X.C., B.S., F.H., Y.S.L., G.P.Z., Z.J.G., S.X.S., H.R.Z., M.Q.Z., and Y.Z., investigation: Q.Z.Y., J.X.C., B.S., F.H., Y.S.L, and G.P.Z, visualization: Q.Z.Y., Q.L., Z.J.G. and B.L.S., funding acquisition: Q.L., S.X.S and B.L.S., project administration: Q.Z.Y., Q.L. and B.L.S., supervision: Q.L., Z.J.G. and B.L.S., writing – original draft: Q.Z.Y. and Q.L., writing – review & editing: Q.L., Q.Z.Y., and B.L.S.

Acknowledgements

This work was financially supported by the National Natural Science Foundation of China (Grant Nos. 52231005 and 51821001).

Conflicts of Interest

The authors declare no conflicts of interest.

Data Availability Statement

The data that support the findings of this study are available from the corresponding author upon reasonable request.

References

1. H. Hou, S. Qian, and I. Takeuchi, "Materials, Physics and Systems for Multicaloric Cooling," *Nature Reviews Materials* 7 (2022): 633–652, https://doi.org/10.1038/s41578-022-00428-x.

2. X. Tang, H. Sepehri-Amin, N. Terada, et al., "Magnetic Refrigeration Material Operating at a Full Temperature Range Required for Hydrogen Liquefaction," *Nature Communications* 13 (2022): 1817.

3. A. Kitanovski, "Energy Applications of Magnetocaloric Materials," *Advanced Energy Materials* 10 (2020): 1903741, https://doi.org/10.1002/aenm.201903741.

4. J. Y. Law, L. M. Moreno-Ramirez, A. Diaz-Garcia, and V. Franco, "Current Perspective in Magnetocaloric Materials Research," *Journal of Applied Physics* 133 (2023): 040903, https://doi.org/10.1063/5.0130035.

5. D. Y. Cong, L. Huang, V. Hardy, et al., "Low-Field-Actuated Giant Magnetocaloric Effect and Excellent Mechanical Properties in a NiMn-Based Multiferroic Alloy," *Acta Materialia* 146 (2018): 142–151, https://doi.org/10.1016/j.actamat.2017.12.047.

6. L. Miao, X. Lu, Z. Wei, Y. Zhang, Y. Zhang, and J. Liu, "Enhanced Mechanical Strength in Hot-Rolled La-Fe-Si/Fe Magnetocaloric Composites by Microstructure Manipulation," *Acta Materialia* 245 (2023): 118635, https://doi.org/10.1016/j.actamat.2022.118635.

7. V. K. Pecharsky and K. A. Gschneidner, "Giant Magnetocaloric Effect in $Gd_5(Si_2Ge_2)$," *Physical Review Letters* 78 (1997): 4494–4497, https://doi.org/10.1103/PhysRevLett.78.4494.

8. T. Krenke, E. Duman, M. Acet, et al., "Inverse Magnetocaloric Effect in Ferromagnetic Ni–Mn–Sn Alloys," *Nature Materials* 4 (2005): 450–454, https://doi.org/10.1038/nmat1395.

9. A. Smith, C. R. H. Bahl, R. Bjork, K. Engelbrecht, K. K. Nielsen, and N. Pryds, "Materials Challenges for High Performance Magnetocaloric Refrigeration Devices," *Advanced Energy Materials* 2 (2012): 1288–1318, https://doi.org/10.1002/aenm.201200167.

10. Q. Wang, Q. Wu, H. Cheng, et al., "Review of the Research on Oxides in Low-Temperature Magnetic Refrigeration," *Journal of the European Ceramic Society* 43 (2023): 6665–6680, https://doi.org/10.1016/j.jeurceramsoc.2023.07.063.

11. M. Falsaperna and P. J. Saines, "Development of Magnetocaloric Coordination Polymers for Low Temperature Cooling," *Dalton Transactions* 51 (2022): 3394–3410, https://doi.org/10.1039/D1DT04073A.

12. Y. Z. Zheng, G. J. Zhou, Z. P. Zheng, and R. E. P. Winpenny, "Molecule-Based Magnetic Coolers," *Chemical Society Reviews* 43 (2014): 1462–1475.

13. F. X. Qin, N. S. Bingham, H. Wang, et al., "Mechanical and Magnetocaloric Properties of Gd-Based Amorphous Microwires Fabricated by Melt-Extraction," *Acta Materialia* 61 (2013): 1284–1293, https://doi.org/10.1016/j.actamat.2012.11.006.

14. L. Shao, L. Xue, Q. Luo, Q. Wang, and B. Shen, "The Role of Co/Al Ratio in Glass-Forming GdCoAl Magnetocaloric Metallic Glasses," *Materialia* 7 (2019): 100419, https://doi.org/10.1016/j.mtla.2019.100419.

15. S. Wei, H. Ge, L. Zhang, H. Shen, F. Cao, and J. Sun, "Tensile Strength Reliability Analysis of GdDyCoAl-based High Entropy Amorphous Microwires," *Materials Letters* 384 (2025): 138130, https://doi.org/10.1016/j.matlet.2025.138130.

16. L. Xue, L. Shao, Z. Li, et al., "Utilization of High Entropy in Rare Earth-Based Magnetocaloric Metallic Glasses," *Journal of Materials Research and Technology* 18 (2022): 5301–5311, https://doi.org/10.1016/j.jmrt.2022.05.022.

17. L. Shao, Q. Luo, M. Zhang, et al., "Dual-Phase Nano-Glass-Hydrides Overcome the Strength-Ductility Trade-Off and Magnetocaloric Bottlenecks of Rare Earth Based Amorphous Alloys," *Nature Communications* 15 (2024): 4159, https://doi.org/10.1038/s41467-024-48531-7.

18. J. Li, L. Xue, W. Yang, C. Yuan, J. Huo, and B. Shen, "Distinct Spin Glass Behavior and Excellent Magnetocaloric Effect in $Er_{20}Dy_{20}Co_{20}Al_{20}RE_{20}$ (RE = Gd, Tb, and Tm) High-Entropy Bulk Metallic Glasses," *Intermetallics* 96 (2018): 90–93, https://doi.org/10.1016/j.intermet.2018.03.002.

19. L. Shao, Q. Wang, L. Xue, et al., "Effects of Minor Si Addition on Structural Heterogeneity and Glass Formation of GdDyErCoAl High-entropy Bulk Metallic Glass," *Journal of Materials Research and Technology* 11 (2021): 378–391, https://doi.org/10.1016/j.jmrt.2021.01.035.

20. L. Xue, L. Shao, Q. Luo, et al., "Liquid Dynamics and Glass Formation of $Gd_{55}Co_{20}Al_{25}$ Metallic Glass with minor Si Addition," *Journal of Materials Science & Technology* 77 (2021): 28–37, https://doi.org/10.1016/j.jmst.2020.11.024.

21. J. Gu, L. Li, Y. Xie, et al., "Turing Structuring with Multiple Nanotwins to Engineer Efficient and Stable Catalysts for Hydrogen Evolution Reaction," *Nature Communications* 14 (2023): 5389, https://doi.org/10.1038/s41467-023-40972-w.

22. Z. Tan, S. Chen, X. Peng, L. Zhang, and C. Gao, "Polyamide Membranes with Nanoscale Turing Structures for Water Purification," *Science* 360 (2018): 518–521, https://doi.org/10.1126/science.aar6308.

23. H. Wang, Q. F. He, X. Gao, et al., "Multifunctional High Entropy Alloys Enabled by Severe Lattice Distortion," *Advanced Materials* 36 (2024): 2305453, https://doi.org/10.1002/adma.202305453.

24. M. Taherijam and H. Abdolvand, "Hydrogen and Hydride Induced Stress Localization in Single Phase HCP and Dual Phase HCP-BCC Alloys," *International Journal of Plasticity* 189 (2025): 104325, https://doi.org/10.1016/j.ijplas.2025.104325.

25. P. Bracconi, E. Pörschke, and R. Lässer, "Investigation of Yttrium and Yttrium Hydride by AES and REELS," *Applied Surface Science* 32 (1988): 392–408, https://doi.org/10.1016/0169-4332(88)90090-6.

26. A. Takeuchi and A. Inoue, "Classification of Bulk Metallic Glasses by Atomic Size Difference, Heat of Mixing and Period of Constituent Elements and Its Application to Characterization of the Main Alloying Element," *Materials Transactions* 46 (2005): 2817–2829, https://doi.org/10.2320/matertrans.46.2817.

27. R. A. Pelcovits, E. Pytte, and J. Rudnick, "Spin-Glass and Ferromagnetic Behavior Induced by Random Uniaxial Anisotropy," *Physical Review Letters* 40 (1978): 476, https://doi.org/10.1103/PhysRevLett.40.476.

28. Q. Luo, B. Schwarz, N. Mattern, and J. Eckert, "Giant Irreversible Positive to Large Reversible Negative Magnetic Entropy Change Evolution in Tb-based Bulk Metallic Glass," *Physical Review B* 82 (2010): 024204, https://doi.org/10.1103/PhysRevB.82.024204.

29. C. A. M. Mulder, A. J. Duyneveldt, and J. A. Mydosh, "Frequency and Field Dependence of the ac Susceptibility of the AuMn Spin-glass," *Physical Review B* 25 (1982): 515, https://doi.org/10.1103/PhysRevB.25.515.

30. Q. Luo, B. Schwarz, N. Mattern, and J. Eckert, "Magnetic Ordering and Slow Dynamics in a Ho-based Bulk Metallic Glass with Moderate Random Magnetic Anisotropy," *Journal of Applied Physics* 109 (2011): 113904, https://doi.org/10.1063/1.3594696.

31. L. Li, K. Nishimura, D. Huo, Z. Qian, and T. Namiki, "Critical Behaviour of the RCo_3B_2 (R=Gd, Tb and Dy) Compounds," *Journal of Alloys and Compounds* 572 (2013): 205–208, https://doi.org/10.1016/j.jallcom.2013.03.270.

32. N. Thi Dung, Y. Pham, D. S. Lam, et al., "Critical Behavior of Polycrystalline $Pr_{0.7}Ca_{0.1}Sr_{0.2}MnO_3$ Exhibiting the Crossover of First and Second Order Magnetic Phase Transitions," *Journal of Materials Research and Technology* 9 (2020): 12747–12755, https://doi.org/10.1016/j.jmrt.2020.09.013.

33. J. Yang, Y. P. Lee, and Y. Li, "Critical Behavior of the Electron-doped Manganite $La_{0.9}Te_{0.1}MnO_3$," *Physical Review B* 76 (2007): 054442, https://doi.org/10.1103/PhysRevB.76.054442.

34. Z. Dong and S. Yin, "Structural, Magnetic and Magnetocaloric Performances in $Cu_{18}Al_{25}Ho_{57}$ and $Cu_{18}Al_{25}Tm_{57}$ Amorphous Ribbons," *Journal of Magnetism and Magnetic Materials* 495 (2020): 165888, https://doi.org/10.1016/j.jmmm.2019.165888.

35. J. Feng, F. Li, G. Wang, J.-Q. Wang, and J. Huo, "Magnetocaloric Effect in Ercu-Based Metallic Glass Composite," *Journal of Non-Crystalline Solids* 536 (2020): 120004, https://doi.org/10.1016/j.jnoncrysol.2020.120004.

36. W. Fu, B. Tang, D. Li, et al., "The Effect of Co Addition on the Enhanced Amorphous Forming Ability and Magnetocaloric Properties of $Gd_{55}Ni_{30}Al_{15}$ Amorphous Alloy," *Journal of Non-Crystalline Solids* 634 (2024): 122968, https://doi.org/10.1016/j.jnoncrysol.2024.122968.

37. W. Gao, X. Wang, L. Wang, Y. Zhang, and J. Cui, "Cryogenic Magnetic Properties of $Er_{60}Ni_{30}Co_{10}$ Amorphous Ribbon," *Journal of Non-Crystalline Solids* 484 (2018): 36–39, https://doi.org/10.1016/j.jnoncrysol.2018.01.010.

38. D. Guo, Y. Zhang, S. Geng, H. Xu, Z. Ren, and G. Wilde, "Structure, Glass-Forming Ability, Magnetic and Cryogenic Magneto-Caloric Properties in the Amorphous $Ni_{30}Co_{10}RE_{60}$ (RE = Ho and Tm) Ribbons," *Journal of Materials Science* 53 (2018): 9816–9822, https://doi.org/10.1007/s10853-018-2257-9.

39. J. Huo, L. Huo, J. Li, et al., "High-Entropy Bulk Metallic Glasses as Promising Magnetic Refrigerants," *Journal of Applied Physics* 117 (2015): 073902, https://doi.org/10.1063/1.4908286.

40. J. Huo, L. Huo, H. Men, et al., "The Magnetocaloric Effect of Gd-Tb-Dy-Al-M (M = Fe, Co and Ni) High-entropy Bulk Metallic Glasses," *Intermetallics* 58 (2015): 31–35, https://doi.org/10.1016/j.intermet.2014.11.004.

41. Q. Luo, P. N. Dinh, X. Kou, and J. Shen, "Controllable Ferromagnetic/Re-Entrant Spin Glass state and Magnetocaloric Response of Gd-Er-Al-Co Metallic Glasses," *Journal of Alloys and Compounds* 725 (2017): 835–839, https://doi.org/10.1016/j.jallcom.2017.06.293.

42. L. Y. Ma, B. Z. Tang, K. C. Chan, et al., "Formability and Magnetic Properties of Dy-Co Binary Amorphous Alloys," *AIP Advances* 8 (2018): 075215, https://doi.org/10.1063/1.5037357.

43. H. Shen, H. Wang, L. Jingshun, et al., "Enhanced Magnetocaloric Properties of Melt-extracted GdAlCo Metallic Glass Microwires," *Journal of Magnetism and Magnetic Materials* 372 (2014): 23–26, https://doi.org/10.1016/j.jmmm.2014.07.024.

44. W. Sheng, J. Q. Wang, G. Wang, J. Huo, X. Wang, and R. W. Li, "Amorphous Microwires of High Entropy Alloys with Large Magnetocaloric Effect," *Intermetallics* 96 (2018): 79–83, https://doi.org/10.1016/j.intermet.2018.02.015.

45. M. N. Song, L. W. Huang, B. Z. Tang, D. Ding, X. Wang, and L. Xia, "Enhanced Curie Temperature and Magnetic Entropy Change of $Gd_{63}Ni_{37}$ Amorphous Alloy by Co Substitution," *Intermetallics* 115 (2019): 106614, https://doi.org/10.1016/j.intermet.2019.106614.

46. S. Uporov, V. Bykov, and N. Uporova, "Magnetocaloric Effect in $Gd_{60}Al_{25}(NiCo)_{15}$ Bulk Metallic Glass," *Journal of Non-Crystalline Solids* 521 (2019): 119506, https://doi.org/10.1016/j.jnoncrysol.2019.119506.

47. J. Wang, P. Zhang, and A. Ning, "Microstructure, Magnetic Properties and Cryogenic Magnetocaloric Effect in $Cu_{20}Al_{20}Er_{60}$ Amorphous Ribbons," *Journal of Magnetism and Magnetic Materials* 465 (2018): 780–783, https://doi.org/10.1016/j.jmmm.2018.05.097.

48. X. Wang, Q. Wang, B. Tang, P. Yu, L. Xia, and D. Ding, "Large Magnetic Entropy Change and Adiabatic Temperature Rise of a Ternary $Gd_{34}Ni_{33}Al_{33}$ Metallic Glass," *Journal of Rare Earths* 39 (2021): 998–1002, https://doi.org/10.1016/j.jre.2020.04.011.

49. L. Xue, L. Shao, Q. Luo, and B. Shen, "$Gd_{25}RE_{25}Co_{25}Al_{25}$ (RE = Tb, Dy and Ho) high-entropy Glassy Alloys with Distinct Spin-Glass Behavior and Good Magnetocaloric Effect," *Journal of Alloys and Compounds* 790 (2019): 633–639, https://doi.org/10.1016/j.jallcom.2019.03.210.

50. Y. Yao, Z. Li, J. Liu, et al., "Effect of Ni Alloying on the Microstructure and Magnetocaloric Properties of Gd-Based Metallic Microfibers," *Journal of Alloys and Compounds* 961 (2023): 170979, https://doi.org/10.1016/j.jallcom.2023.170979.

51. H. Yin, Y. Huang, Y. Bao, et al., "Comparable Magnetocaloric Properties of Melt-Extracted $Gd_{36}Tb_{20}Co_{20}Al_{24}$ Metallic Glass Microwires," *Journal of Alloys and Compounds* 815 (2020): 150983, https://doi.org/10.1016/j.jallcom.2019.06.085.

52. J. Zhu, Q. Luo, M. Cai, B. Ji, and B. Shen, "Magnetocaloric Performance and Its Linear Relationship with Magnetoresistance in Gd-Al-Cu Metallic Glass," *Journal of Magnetism and Magnetic Materials* 507 (2020): 166828, https://doi.org/10.1016/j.jmmm.2020.166828.

53. H. Sun, J. F. Wang, L. Tian, et al., "Magnetic Properties and Magnetocaloric Effect in $RE_{55}Co_{30}Al_{10}Si_5$ (RE = Er and Tm) Amorphous Ribbons," *Chinese Physics B* 31 (2022): 117503, https://doi.org/10.1088/1674-1056/ac8733.

54. Y. K. Zhang, J. Zhun, S. Li, et al., "Glass Forming Ability, Magnetic Properties and Cryogenic Magnetocaloric Effects in $RE_{60}Co_{20}Al_{20}$ (RE = Ho, Er, Tm) Amorphous Ribbons," *Journal of Alloys and Compounds* 895 (2022): 162633, https://doi.org/10.1016/j.jallcom.2021.162633.

55. Y. K. Zhang, D. Gao, B. B. Wu, et al., "Magnetic Properties, Magnetocaloric Effect and Refrigeration Performance in $RE_{60}Al_{20}Ni_{20}$ (RE = Tm, Er and Ho) Amorphous Ribbons," *Journal of Applied Physics* 127 (2020): 033905, https://doi.org/10.1063/1.5140765.

56. F. Zhang, I. Batashev, Q. Shen, et al., "Impact of F and S Doping on $(Mn,Fe)_2(P,Si)$ Giant Magnetocaloric Materials," *Acta Materialia* 234 (2022): 118057, https://doi.org/10.1016/j.actamat.2022.118057.

57. H. B. Zhou, Z. B. Yu, F. Hu, et al., "Emergence of Invar Effect with Excellent Mechanical Property by Electronic Structure Modulation in $LaFe_{11.6-x}Co_xSi_{1.4}$ Magnetocaloric Materials," *Acta Materialia* 260 (2023): 119312, https://doi.org/10.1016/j.actamat.2023.119312.

58. X. C. Zhong, D. R. Peng, X. T. Dong, et al., "Improvement in Mechanical and Magnetocaloric Properties of Hot-Pressed $La(Fe,Si)_{13}/La_{70}Co_{30}$ Composites by Grain Boundary Engineering," *Materials Science and Engineering: B* 263 (2021): 114900, https://doi.org/10.1016/j.mseb.2020.114900.

59. X. Miao, C. Wang, T. Liao, et al., "Novel Magnetocaloric Composites with Outstanding Thermal Conductivity and Mechanical Properties Boosted by Continuous Cu Network," *Acta Materialia* 242 (2023): 118453, https://doi.org/10.1016/j.actamat.2022.118453.

60. O. Glushko, A. Funk, V. Maier-Kiener, et al., "Mechanical Properties of the Magnetocaloric Intermetallic $LaFe_{11.2}Si_{1.8}$ Alloy at Different Length Scales," *Acta Materialia* 165 (2019): 40–50, https://doi.org/10.1016/j.actamat.2018.11.038.

61. S. Kavita, M. Alagusoundarya, V. V. Ramakrishna, et al., "On the Table-Like Magnetocaloric Effect, Microstructure and Mechanical Properties of $La_xFe_{11.6}Si_{1.4}$ System," *Journal of Alloys and Compounds* 895 (2022): 162597, https://doi.org/10.1016/j.jallcom.2021.162597.

62. B. Y. Song, Y. Q. Han, J. Cheng, et al., "Effect of Al Doping on Magnetocaloric Effect and Mechanical Properties of $La(FeSi)_{13}$-based Alloys," *Journal of Alloys and Compounds* 990 (2024): 174398, https://doi.org/10.1016/j.jallcom.2024.174398.

63. X. C. Zhong, X. L. Feng, J. H. Huang, et al., "A Bimodal Particle Size Distribution Enhances Mechanical and Magnetocaloric Properties of Low-temperature Hot Pressed Sn-bonded $La_{0.8}Ce_{0.2}(Fe_{0.95}Co_{0.05})_{11.8}Si_{1.2}$ Bulk Composites," *Journal of Magnetism and Magnetic Materials* 469 (2019): 133–137, https://doi.org/10.1016/j.jmmm.2018.08.053.

64. M. Zhang, Y. Shao, C. Li, et al., "High-Performance $LaFe_{11.6}Si_{1.4}H$/Al Composites for Magnetic Refrigeration: a Good Combination of Magnetocaloric Effect, Mechanical Properties, and Thermal Conductivity," *Journal of Alloys and Compounds* 962 (2023): 171123, https://doi.org/10.1016/j.jallcom.2023.171123.

65. S. Sun, J. Bai, J. Gu, et al., "Extraordinary Mechanical Properties and Room-temperature Magnetocaloric Effects in Spark Plasma Sintered All-d-metal Ni-Co-Mn-Ti Alloy," *Journal of Alloys and Compounds* 976 (2024): 173406, https://doi.org/10.1016/j.jallcom.2023.173406.

66. W. H. Wang, Z. G. Zheng, C. F. Li, Y. Hong, L. Lei, and D. C. Zeng, "Effect of Cu and B Co-doping on Magnetocaloric Effect, Phase Transition, and Mechanical Properties of $Mn_{1.05}Fe_{0.9}P_{0.5}$-$Si_{0.5}Cu_{0.10}B$ Alloys," *Journal of Magnetism and Magnetic Materials* 517 (2021): 167380, https://doi.org/10.1016/j.jmmm.2020.167380.

67. Y. Kuang, Z. Ai, B. Yang, et al., "Simultaneously Achieved Good Mechanical Properties and Large Magnetocaloric Effect in Spark Plasma Sintered Ni-Mn-In Alloys," *Intermetallics* 124 (2020): 106868, https://doi.org/10.1016/j.intermet.2020.106868.

68. S. Kavita, V. V. Ramakrishna, S. Behara, et al., "Investigation of Magnetocaloric and Mechanical Properties of $Ni_{49-x}Mn_{39}Sb_{12}Co_x$ Alloys," *Journal of Alloys and Compounds* 847 (2020): 156558, https://doi.org/10.1016/j.jallcom.2020.156558.

69. J. Bai, D. Liu, J. Gu, et al., "Excellent Mechanical Properties and Large Magnetocaloric Effect of Spark Plasma Sintered Ni-Mn-In-Co Alloy," *Journal of Materials Science & Technology* 74 (2021): 46–51, https://doi.org/10.1016/j.jmst.2020.10.011.

70. Y. C. Zhang, V. Franco, Y. F. Wang, H. X. Peng, and F. X. Qin, "Microstructure, Magnetism and Critical Behavior of Hot Pressed Ni-Mn-Ga/Al Magnetocaloric Composites with Enhanced Thermal Conductivity and Mechanical Properties," *Journal of Alloys and Compounds* 918 (2022): 165664, https://doi.org/10.1016/j.jallcom.2022.165664.

71. Z. G. Zheng, X. L. Chen, H. Y. Wang, et al., "Giant Magnetocaloric Effects of MnNiSi-Based High-Entropy Alloys near Room Temperature," *Journal of Alloys and Compounds* 966 (2023): 171483, https://doi.org/10.1016/j.jallcom.2023.171483.

72. J. Kim, D. Hall, H. Yan, et al., "Roughening Improves Hydrogen Embrittlement Resistance of Ti-6Al-4 V," *Acta Materialia* 220 (2021): 117304, https://doi.org/10.1016/j.actamat.2021.117304.

73. S. H. Li, D. H. Lee, Y. Zhao, and U. Ramamurty, "Hydrogen-induced Softening and Embrittlement in 316L Stainless Steel Fabricated Using Laser-powder Bed Fusion," *Acta Materialia* 274 (2024): 119959, https://doi.org/10.1016/j.actamat.2024.119959.

74. D. Granata, E. Fischer, and J. F. Löffler, "Effectiveness of Hydrogen Microalloying in Bulk Metallic Glass Design," *Acta Materialia* 99 (2015): 415–421, https://doi.org/10.1016/j.actamat.2015.08.001.

75. S. Balachandran, J. Orava, M. Köhler, et al., "Elemental Re-Distribution Inside Shear Bands Revealed by Correlative Atom-Probe Tomography and Electron Microscopy in a Deformed Metallic Glass," *Scripta Materialia* 168 (2019): 14–18, https://doi.org/10.1016/j.scriptamat.2019.04.014.

76. J. J. Lewandowski and A. L. Greer, "Temperature Rise at Shear Bands in Metallic Glasses," *Nature Materials* 5 (2006): 15–18, https://doi.org/10.1038/nmat1536.

77. J. M. D. Coey, "Amorphous Magnetic Order," *Journal of Applied Physics* 49 (1978): 1646–1652, https://doi.org/10.1063/1.324880.

78. J. Y. Law, V. Franco, L. M. Moreno-Ramirez, et al., "A Quantitative Criterion for Determining the Order of Magnetic Phase Transitions Using the Magnetocaloric Effect," *Nature Communications* 9 (2018): 2680, https://doi.org/10.1038/s41467-018-05111-w.

79. G. Wu, K. C. Chan, L. Zhu, L. Sun, and J. Lu, "Dual-phase Nanostructuring as a Route to High-Strength Magnesium Alloys," *Nature* 545 (2017): 80–83, https://doi.org/10.1038/nature21691.

80. Y. Suo, Q. Liu, Y. Yin, Y. Lv, B. Wang, and X. Zhao, "Investigation on the Mechanism of the Load Transfer Behavior in Particle-reinforced Metal Matrix Composites," *Journal of Materials Research* 40 (2025): 250–264, https://doi.org/10.1557/s43578-024-01498-z.

81. D. Jang and J. R. Greer, "Transition from a Strong-yet-Brittle to a Stronger-and-Ductile State by Size Reduction of Metallic Glasses," *Nature Materials* 9 (2010): 215–219, https://doi.org/10.1038/nmat2622.

82. B. Cheng and J. R. Trelewicz, "Mechanistic Coupling of Dislocation and Shear Transformation Zone Plasticity in Crystalline-Amorphous Nanolaminates," *Acta Materialia* 117 (2016): 293–305, https://doi.org/10.1016/j.actamat.2016.07.011.

83. A. C. Lund and C. A. Schuh, "Strength Asymmetry in Nanocrystalline Metals under Multiaxial Loading," *Acta Materialia* 53 (2005): 3193–3205, https://doi.org/10.1016/j.actamat.2005.03.023.

84. M. Grewer and R. Birringer, "Shear Shuffling Governs Plastic Flow in Nanocrystalline Metals: an Analysis of Thermal Activation Parameters," *Physical Review B* 89 (2014): 184108, https://doi.org/10.1103/PhysRevB.89.184108.

Supporting Information

Additional supporting information can be found online in the Supporting Information section.

Supporting File 1: adfm74557-sup-0001-SuppMat.docx.

Supporting File 2: adfm74557-sup-0002-VideoS1-S5.zip.